Arabian Journal for Science and Engineering (2023) 48:11333–11350
https://doi.org/10.1007/s13369-022-07424-x

RESEARCH ARTICLE-MECHANICAL ENGINEERING

Numerical Modelling and Entropy Analysis of Pitching Aerofoil Under the Dynamic Stall

Amit Varakhedkar[1] · **Rajendran Senthil Kumar**[1]

Received: 26 July 2022 / Accepted: 24 October 2022 / Published online: 8 November 2022

Abstract
In this research, the improvement of wind turbine blade undergoing pitching motion by means of identifying optimized aerofoil profile has been studied as a crucial part of enhancing effectiveness of wind energy turbine system. Here, the projected air is considered as unidirectional with flow speed range of Re $5*10^5$ to 10^6. The effect of different pitching aerofoil blade profiles ranging from NACA 0012, S-809, and SD 7062 has been investigated in addition to the aerodynamic characteristics, entropy generation in the flow and exergy which are also proposed as a criterion for selecting optimum design for the oscillating aerofoil blade. Finally, increment in Re shows increase in the entropy generation rate and decrease in exergy efficiency. Consequently, aerofoil profile shows prominent variations in exergy with SD 7062 experiencing least entropy generation rate and exergy efficiency of around 93% due to its streamlined profile as compared to other profiles in this study. Meanwhile, NACA 0012 experiences minimum exergy efficiency of around 39% for Re 10^6.

Keywords Dynamic stall · Aerofoil pitching · Wind turbine · Entropy generation rate · Numerical Simulation

List of Symbols

C	Chord length [m]
C_D	Coefficient of drag
C_L	Coefficient of lift
$\dot{E}$	Exergy [W]
I	Irreversibility [W/m^3]
I_l	Local entropy generation
K	Reduced frequency
k	Turbulence kinetic energy [m^2/s^2]
P	Pressure [Pa]
Re	Reynolds number
S_G	Total entropy generation rate [W/K]
S_{gen}	Local entropy generation rate [W/(m^{3}K)]
S_x	Source term for body force-x
S_y	Source term for body force-y
t	Flow time [s]
T_0	Reference temperature [K]
u	Stream-wise velocity [m/s]
u_∞	Free-stream velocity [m/s]
v	Cross-stream velocity [m/s]
x	Stream-wise dimension of coordinates [m]
y	Cross-stream dimension of coordinates [m]
y +	Non-dimensional wall distance

Greek Symbols

α	Angle of attack [deg]
α_{mean}	Mean α [deg]
α_{amp}	Amplitude α [deg]
ϵ	Turbulence dissipation rate [m^2/s^2]
ρ	Density of fluid [kgm^{-3}]
τ_{ij}	Shear stress tensor
μ	Viscosity of fluid [Pa s]
μ_t	Turbulent viscosity [Pa s]
ω	Angular frequency [rad/s
NACA	National Advisory Committee for Aeronautics
NREL	National renewable energy laboratory
SIMPLE	Semi-implicit method for pressure-linked equations
SST	Shear stress transport

✉ Rajendran Senthil Kumar
senthilr2@srmist.edu.in

[1] Department of Mechanical Engineering, SRM Institute of Science and Technology, Kattankulathur 603 203, India

Abbreviations

NACA	National Advisory Committee for Aeronautics
NREL	National renewable energy laboratory
SIMPLE	Semi-implicit method for pressure-linked equations
SST	Shear stress transport

1 Introduction

The natural wind has strong shear and various velocity magnitude and directions, causing the dynamic stall phenomena in a horizontal axis wind turbine (HAWT). Dynamic stall is a nonlinear and unsteady aerodynamic effect associated with flow separation and reattachment, further causing dynamic blade loading and variable performance. The phenomena of dynamic stall occur after the static stall angle, usually due to rapid variations within the angle of attack or due to the unsteady motion of the wind. The dynamic stall phenomena cannot be prevented, but a comprehensive study of unsteady aerodynamics will be crucial in suppressing its effects and assisting the modification of wind turbine blade design. Various experimental methods and numerical models are developed to predict the aerodynamic loads and complex flow conditions during the dynamic stall phenomena. Zhao et al. [1] performed the simulation for modelling and analysis of a single blade installation on the hub of an onshore wind turbine. The significant finding from the research was for a lifted blade, the aerodynamic loads undergoing oscillatory motion were dominant on the middle and root part of the blade. Furthermore, the sway and roll motions are predominant on the blades, leading to pendulum motion of a blade. Castellaini et al. [2] utilized SCADA control system for the analysis of the angular orientation of the wind turbine. They explore the potential of the wind turbine blades functioning on the response and feedback basis for aligning the ideal angle of attack. A design optimization framework for the oscillating aerofoil was obtained by Li et al. [3] to minimize acoustic noise for high aerofoil efficiency. Liu et al. [4] developed reduced-order methods for unsteady aerodynamic prediction of pitching aerofoil. This method was more effective than Lattice Boltzmann methods while requiring lesser computational expense than CFD models. Yan and Archer [5] focussed on the compressibility effects, particularly the variable density, and obtained its performance parameter for determining its effect on the dynamic stall and turbulence. Chan et al. [6] optimized the wind turbine blades from the Savonius to the aerofoil blades using CFD codes and analytical algorithms. Werner et al. [7] performed experimental analysis to determine the dynamic stall of aerofoil blade using particle image velocimetry and laser sheet detection. The experimentation was performed for NACA 0012 at Re $3.73*10^5$ for varying angles ranging from 5 to 20 degrees. Soltani and Mahmoudi [8] performed the experiment for NACA 0012 for aerofoil pitching at Re $8.5*10^5$. The results obtained from the paper were in the estimation of the dependency of frequency and amplitude on the dynamic stall.

The previous research dealt with incorporating numerical simulation towards a practical application of a single-bladed HAWT experiencing steady and dynamic behaviour. Due to the excess of computational expenditure, simulations are being performed on an oscillating aerofoil to study the pitching motion of a HAWT blade. A wide range of research has been done on oscillating frequency effects and angle of attack variations for a pitching aerofoil on the dynamic stall. Akbari and Prince [9] have used a numerical approach for estimating the reduced frequency and Reynolds number on dynamic stall for a NACA 0012. Their observations show that the oscillation delay in the static stall as the angle of attack was postponed. Vortex formation on the rear region leads to higher lift forces acting on the blades. For higher angles of flow separation, larger wake zones were observed. The effect of pitch angle on power requirement and aerodynamics was studied by Rezaeiha et al. [10] for a vertical axis wind turbine (VAWT). A slight variation of 2 degrees pitch angle caused an increase in pressure coefficient by 6.6%. Cui and Knight [11] developed a solver for computing the pitching motion in the subsonic range for higher values of non-dimensional pitching rate in the range of $k = 0.2$ to 0.4. The process of stall reduction for aerofoil pitching has been carried out in the following research, Gharali and Johnson [12–14], on a NACA 0012 aerofoil undergoing pitching motion at the range for Re 10^5. The oscillating aerofoil blade experienced additional yaw loading when it was exposed to an unsteady sinusoidal wind. The phase angle between the wind and aerofoil oscillation was initially kept the same and then varied to 180 degrees. The dynamic loading was more substantial for phase angles lesser than 90 degrees. Gharali [15] expanded the previous research work for different profiles of aerofoil blades that were more popular in wind turbine applications. Gharali and Johnson [16] also compared the turbulence models, k-epsilon (Resizable) and k-omega (SST), in the accurate estimation of dynamic stall. The k-omega (SST) turbulent model was determined to produce an optimum model for its accurate estimation of strain rate. The latter was selected due to its high-end predictivity of the turbulent wake along the aerofoil as depicted by Wilcox [17]. This turbulence model can adjust its equation from k-epsilon near the walls to predict viscous turbulence determination and k-omega for predicting downstream wake [18]. Xu et al. [19] developed a method to contain the dynamic wake generated using two co-flow jets, one with the pressure and one along the suction side. This reduced the dynamic stall and drag coefficient and increased

lift coefficient for S809 aerofoil. The study of blade vibration for S809 aerofoil for translation and pitching motion was conducted by Liu et al. [20]. An aerodynamic model on blade element-momentum was revised to account for vibration-induced velocity components on the aerodynamic loads for the accurate estimation of the dynamic stall.

The entropy generation is a relatively new term for determining the irreversibility of the system and determining the performance efficiencies of turbo-machines. The concept of entropy generation was introduced by Bejan [21, 22]. The entropy generation occurred due to heat transfer being the primary source of irreversibility. The main objective was for the entropy generation minimization in the system for increasing the efficiency of a process. The thermodynamics' second law analysis was further carried out for a plate exchanger [23] using the potential entropic concept. The entropic potential loss number was introduced that incorporated the second law efficiency for numerical assessment. The analytical equations for entropy generation rate given by Bejan [21] remain the base for entropy generation rate, which has been utilized in various cases, particularly for the performance effect of wind turbines. Vatanmakan et al. [24] determined the energy trapped by the flow separation due to irreversibility for a stationery cascade of the turbine using numerical method. Walsh and McEligot [25] derived an entropy generation relation for turbulent wall layer flows. The entropy generation calculations were coupled with the wall laws to account for the shear layer disturbances at low-pressure gradients near the wall. A similar study involving geometrical optimization of an ejector in a wet stream ejector from a refrigeration cycle has been carried out using entropy generation method [26]. Shehata et al. [27] performed a parametric study on estimating entropy generation rate for the four aerofoils, including NACA 0015, 0012, 0020, and 0021. The NACA 0015, because of its geometrical nature, was obtained to produce the least entropy generation rate. Wen et. al. [28] obtained exergy loss and destruction characteristics of wind turbine using particle image velocimetry and finite element method. Using weight analysis methods, five design parameters influencing exergy efficiency were analysed of which optimizing wind turbine capacity required optimizing slot structure and air gap length. Mortaza and Sobhgali [29] further performed simulations on the NREL series of aerofoil blades. They derived a second-order efficiency model using the entropy generation data, which was further used as a parameter to determine the turbine's performance for the blade. Mamouri et al. [30] performed a similar study for the most widely applied commercial aerofoils, including NREL S809, S822, and SD7022 aerofoils. Mamouri et al. [31] further studied the influence of the oscillating frequency on the entropy generation and second-order efficiency of a pitching aerofoil blade, which was found out to be negligible for total entropy generation. The study also established the effectivity of the entropy generation model in the estimation of dynamic stall against the traditional methods based on the aerodynamic loads. Mamouri et al. [32] also performed an experimental study on the pitching aerofoil on different reduced frequencies. The aerodynamic loads showed oscillatory behaviour, which resulted in increased fatigue tension on aerofoils. Furthermore, the entropy generation method was utilized to obtain a corrected aerofoil profile.

In this paper, the influence of different aerofoil blade profiles, Reynolds number, and unsteady angle of attack is studied on the entropy generation rate of a wind turbine aerofoil blade undergoing pitching motion. The dynamic stall characteristics of aerofoils NACA 0012, NREL S8090, and SD 7062 have been simulated. Finally, the behaviour of the vorticity field, unsteady turbulent wake formation, and aerodynamic coefficients are provided in detail in connection with the entropy generation rate. The present study has also incorporated the turbulent energy distribution and entropy generation rate data towards calculating exergy efficiency.

2 Problem Statement

The geometrical influence on fluid flow characteristics is essential in roto-dynamic members and machinery. The present study prefers three different aerofoil profiles such as *NACA-0012*, *NREL S-809,* and *SD7062* for detailed analysis. Air is considered as the working fluid with density 1 kg/m^{3}and viscosity 10^{-6} Pa s, for a Reynolds number range 5×10^5 to 10^6 where the dynamic stall phenomena is dominant. NACA-0012 is widely used due to its symmetrical profile and easy machinery, whereas the other profiles are also used substantially for the application of wind turbines [33, 34]. The low Reynolds number range used in the study is preferred for dynamic stalling [13].

The physical problems have been modelled, and the computational domain is shown in Fig. 1. The dimensions of the domain have been expressed in terms of aerofoil chord length (C) to ensure a wide range of applicability. The Reynolds number (Re) is a function of free-stream velocity, the chord length, and the fluid properties.

$$\mathrm{Re} = \frac{\rho u_\infty C}{\mu} \tag{1}$$

The rectangular domain size is 40C × 60C with a revolving zone radius of 6C (Fig. 2). The aerofoil blade will be in pitching motion, where the angle of attack (α) will be a sinusoidal function of time (t) along its aerodynamic centre. The aerodynamic centre is taken to be at a distance of C/4 from the aerofoil tip along the centreline. Even though the literature reports [30] that the oscillating frequency does not have any influence on total entropy generation, the present study

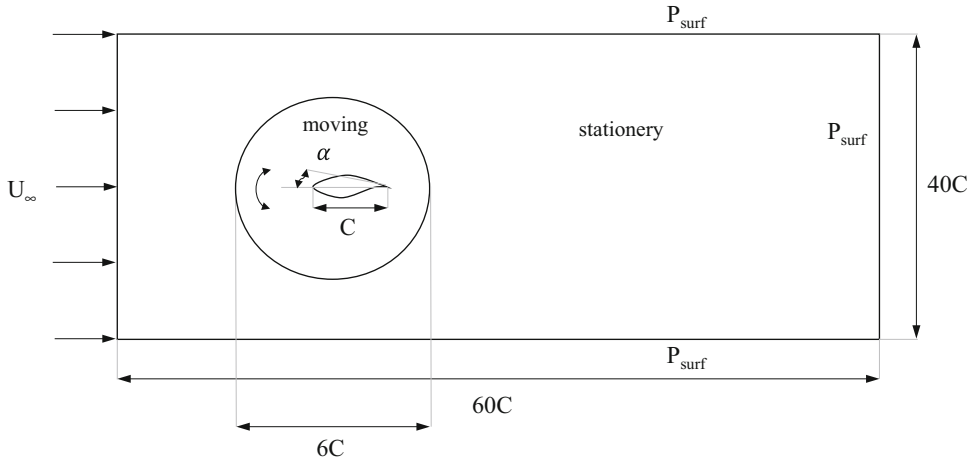

Fig. 1 Schematic layout of aerofoil pitching

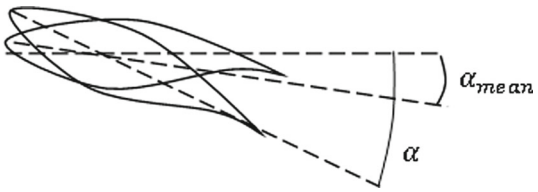

Fig. 2 Aerofoil pitching motion

vigorously investigates the entropy generation and exergy efficiency by mainly focussing the turbulence effects, wake behaviours, and vortex strain rate into account for accurate estimation of dynamic stalling and exergy distribution. The dynamic stall has been studied for a reduced frequency of $K = 0.026$. This reduced frequency has been widely selected in previous works [33, 35]. The reduced frequency is calculated using,

$$K = \frac{\omega C}{2u_\infty} \tag{2}$$

where ω is the angular frequency of the aerofoil along the aerodynamic centre. The equation of pitching motion of the aerofoil is given by Gharali and Johnson 2012 [16],

$$\alpha = \alpha_{\text{mean}} + \alpha_{\text{amp}}\sin(\omega t) \tag{3}$$

where the α_{mean} is the mean angle of the profile and α_{amp} is the magnitude of the maximum variation of the aerofoil blade with respect to time. For the present study, α_{mean} is taken as 8° and the fluctuating angle, α_{amp} is 10.6°, similar to the previous experimental and numerical validated work [35, 36]. The aerofoil pitching motion is shown in Fig. 2.

The domain is divided into moving and stationary zones. The inner circular zone or the moving zone is the only part that will engage in dynamic motion. The stationery zone is where the boundary conditions will act. The two zones are separated by an interface. This subdivision of zones or the moving reference frame has been dealt with effectively applying unsteady motion near the required zones for effective results and less computational dependency [37, 38].

3 Governing Equations

The two-dimensional domain is preferred for simulations due to its low computational requirement, and there was a negligible result variation as shown by [26]. The unsteady Navier–Stokes equations are considered for solving the two-dimensional flows. The continuity and momentum equations used in the simulations are shown below [39].

Continuity equation:

$$\frac{\delta\rho}{\delta t} + \left(\frac{\partial u}{\partial x} + \frac{\partial v}{\partial y}\right) = 0 \tag{4}$$

Momentum (X) equation:

$$\rho\frac{\partial u}{\partial t} + \rho\left(u\frac{\partial u}{\partial x} + v\frac{\partial u}{\partial y}\right) = -\frac{\partial p}{\partial x} + \mu\left(\frac{\partial^2 u}{\partial x^2} + \frac{\partial^2 u}{\partial y^2}\right) - \left[\frac{\delta\left(\overline{\rho u'^2}\right)}{\delta x} + \frac{\delta\left(\overline{\rho u' v'}\right)}{\delta y}\right] + S_x \tag{5}$$

Momentum (Y) equation:

$$\rho\frac{\partial v}{\partial t} + \rho\left(u\frac{\partial v}{\partial x} + v\frac{\partial v}{\partial y}\right) = -\frac{\partial p}{\partial y} + \mu\left(\frac{\partial^2 v}{\partial x^2} + \frac{\partial^2 v}{\partial y^2}\right) - \left[\frac{\delta\left(\overline{\rho v'^2}\right)}{\delta y} + \frac{\delta\left(\overline{\rho u' v'}\right)}{\delta x}\right] + S_y \tag{6}$$

The above equations are solved by a suitable turbulence model to obtain the desired result. The k-ω SST is used for

solving turbulent flow [40]. The SST k − ω model is capable of capturing the flow structures of dynamic aerofoils associated with leading edge vortex formations for a wide range of Reynolds numbers with an acceptable accuracy [16, 17]. Although this model was prepared for fully turbulent flows, it can accommodate transition regime by incorporating a low Re correlation [18] which is ideal for the Re range used in the present study. The SST k − ω model is preferred over the resizable k-ϵ and the Wilcox k- ω due to its effectiveness in the flow disturbance. This model has higher accuracy for the flows in further wake regions [23] as the flow shear rate is a crucial parameter in determining entropy generation rate. The equation for k-ω SST consists of the equations for turbulent kinetic energy (k) and specific dissipation rate (ω). [17]

Turbulent kinetic energy:

$$\frac{\partial(\rho k)}{\partial t}+\frac{\partial(\rho v k)}{\partial y}=P-\beta^{*}\rho\omega k+\frac{\partial}{\partial y}\left[(\mu+\sigma_k\mu_t)\frac{\partial k}{\partial y}\right] \quad (7)$$

Specific dissipation rate:

$$\frac{\partial(\rho\omega)}{\partial t}+\frac{\partial(\rho v\omega)}{\partial y}=\frac{\gamma}{\vartheta_t}P-\beta\rho\omega^{2}+\frac{\partial}{\partial y}\left[(\mu+\sigma_\omega\mu_t)\frac{\partial\omega}{\partial y}\right]+2(1-F_1)\frac{\sigma_{\omega2}\rho}{\omega}\frac{\partial k}{\partial y}\frac{\partial\omega}{\partial y} \quad (8)$$

The variables assigned in these equations are referred from [19], where

$$P=\tau_{ij}\frac{\delta u_i}{\delta x_j} \quad (9)$$

$$\tau_{ij}=\mu_t\left(2S_{ij}-\frac{2}{3}\frac{\delta u_k}{\delta x_k}\delta_{ij}\right)-\frac{2}{3}\rho k\delta_{ij} \quad (10)$$

$$S_{ij}=0.5\left(\frac{\delta u_i}{\delta x_j}+\frac{\delta u_j}{\delta x_i}\right) \quad (11)$$

$$\mu_{\mathrm{t}}=\frac{\rho\alpha_1 k}{\max(\alpha_1\omega,\prod F_2)} \quad (12)$$

$$\varphi=F_1\varphi_1+(1-F_1)\varphi_2 \quad (13)$$

$$F_1=\tanh\left(\epsilon^{4}\right) \quad (14)$$

$$\epsilon=\min\left(\max\left(\frac{\sqrt{k}}{0.09\omega y_n};\frac{500\mu_i}{\rho y_n^{2}\omega}\right);\frac{4\rho\sigma_{\omega2}k}{CD_{k\omega}y_n^{2}}\right) \quad (15)$$

$$CD_{k\omega}=\max\left(2\rho\sigma_2\frac{1}{\omega}\frac{\delta k}{\delta y}\frac{\delta\omega}{\delta y};10^{-20}\right) \quad (16)$$

The constants in this model are as follows:

$$\sigma k_1=0.85,\ \sigma_{\omega1}=0.65,\ \beta_1=0.075;$$

$$\sigma k_2=1,\ \sigma_{\omega2}=0.856,\ \beta_2=0.0828; \quad (17)$$

$$\beta^{*}=0.09,\ \alpha_1=0.31$$

The value of F_1 varies from 0 to 1 on moving away from the wall.

The local viscous entropy generation rate is captured using equation [31, 41, 42].

$$S_{\mathrm{gen}}=\frac{(\mu+\mu_t)}{T_o}\left[2\left(\left(\frac{\partial\overline{u}}{\partial x}\right)^{2}+\left(\frac{\partial\overline{v}}{\partial y}\right)^{2}\right)+\left(\frac{\partial\overline{u}}{\partial y}+\frac{\partial\overline{v}}{\partial x}\right)^{2}\right]+\frac{\rho\varepsilon}{T_o} \quad (18)$$

This is a mathematical derived expression for the analytical solutions given by Bejan [21] on entropy generation. Local entropy generation I_l and irreversibility I are defined as

$$I_{\mathrm{l}}=T_0S_{\mathrm{gen}} \quad (19)$$

$$I=T_0S_{\mathrm{G}}$$

where S_{G} represents total entropy generation rate for the control volume.

$$S_{\mathrm{G}}=\iiint S_{\mathrm{gen}}dV \quad (20)$$

The drag and lift parameters are calculated from (20–21).

$$C_{\mathrm{D}}=\frac{F_{\mathrm{D}}}{\rho{u_\infty}^{2}C} \quad (21)$$

$$C_{\mathrm{L}}=\frac{F_{\mathrm{L}}}{\rho{u_\infty}^{2}C} \quad (22)$$

The effective work done (W_{out}) is defined as the network done by the aerofoil blade in displacing the air [31, 32]. The equation for W_{out} is given by,

$$W_{\mathrm{out}}=\overrightarrow{F_L}\times\overrightarrow{v} \quad (23)$$

The equation is obtained by assuming that the entire energy given to the system is converted into useful work. The exergy efficiency (ϵ) [29] or the second law efficiency, which computes the effectiveness of the system based on its performance in reversible systems, is defined as

$$\epsilon=\frac{\dot{E}x_{\mathrm{prod}}}{\dot{E}x_{\mathrm{out}}-\dot{E}x_{\mathrm{in}}} \quad (24)$$

where $\dot{E}x_{\mathrm{prod}}$ is defined as the exergy produced due to the lift force in the aerodynamics aspect. Also, the $\dot{E}x_{\mathrm{out}}-\dot{E}x_{\mathrm{in}}$

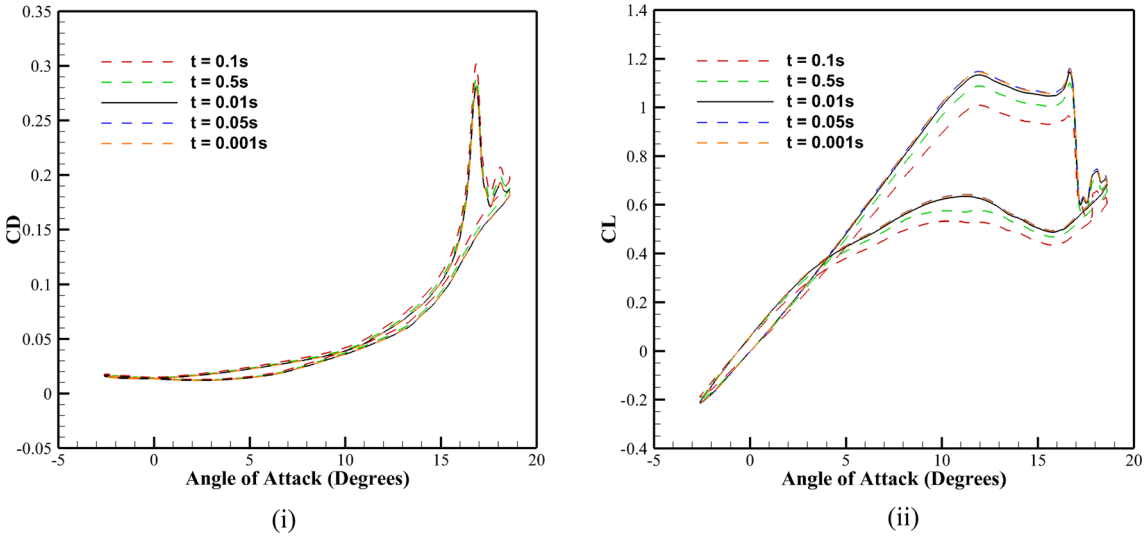

Fig. 3 Time-step optimization (i) Coefficient of drag (ii) coefficient of lift

is defined as the summation of the exergy of useful work, destruction, and losses. [29] assumed the exergy of destruction is considered zero, which gives the following term.

$$\dot{E}x_{\text{out}} - \dot{E}x_{\text{in}} = \dot{E}x_{\text{work}} + \dot{E}x_{\text{loss}} = W_{\text{out}} + T_0 S_G \tag{25}$$

The exergy efficiency can be rewritten as follows:

$$\epsilon = \frac{W_{\text{out}}}{W_{\text{out}} + T_0 S_G} \tag{26}$$

4 Numerical Solution

All simulations have been carried out using the commercial software ANSYS Fluent [43]. The dynamic motion of pitching is imparted to the moving mesh using a user-defined function over the moving zone. The pressure and velocity couplings have been performed using SIMPLE algorithm. Second order—upwind scheme for spatial discretization, and first order—upwind scheme for temporal discretization. Since the study involves unsteady flows, time-step optimization is important to maintain temporal accuracy. The time-step (t) study was performed for 0.1, 0.05, 0.01, 0.005, and 0.001 s S809 aerofoil exposed to a free stream of Re 10^6 (Fig. 3). The time-step size with 0.01 s was considered ideal for capturing the dynamic wake behaviour and which required minimum computational efforts.

5 Grid Generation

The mesh is divided into internal and external zones, separated by an interface. The external zone utilizes a structured mesh which becomes fine while transitioning to the boundaries near the interface. The interior (Fig. 4). The interior zone has unstructured mesh, and the element size is constant throughout to effectively capture the vortices formed. Grid sensitivity study was performed on aerofoils S809 for Re 10^6 over three mesh of varying number of elements: Mesh 1 (88,888 cells), Mesh 2 (99,999 cells), and Mesh 3 (110,000 cells). Due to the overlapping of the curves of Mesh 2 and 3 for lift and drag coefficients (Fig. 5), Mesh 2 has been utilized for the further study. Along the aerofoils, 400 nodes were distributed with high resolution on the leading and trailing edge of the aerofoils for all meshes. In addition, 600 nodes are distributed along with the interface. The thickness of cells around the aerofoils blade was maintained at y + < 1 which is the prescribed range for k-ω (SST) model [39]. Figure 6 shows the variation of y + with respect to the curve length for S-822 aerofoils, where the value was achieved lesser than 1 throughout the aerofoils profile.

6 Result and Discussion

6.1 Validation of results

The results were compared with the available numerical and experimental data for the aerodynamic coefficients at different angles of attack (Fig. 7). The case was formulated in accordance with the experimental results obtained from Ramsay et al. [44] for aerofoils S 809. Numerical data were validated with the BL method imposed by Gupta and Leishman [35]. Gharali and Johnson [19] and Mamouri et al. [32] have performed simulations using SST turbulence model for different numerical setups are compared them as well.

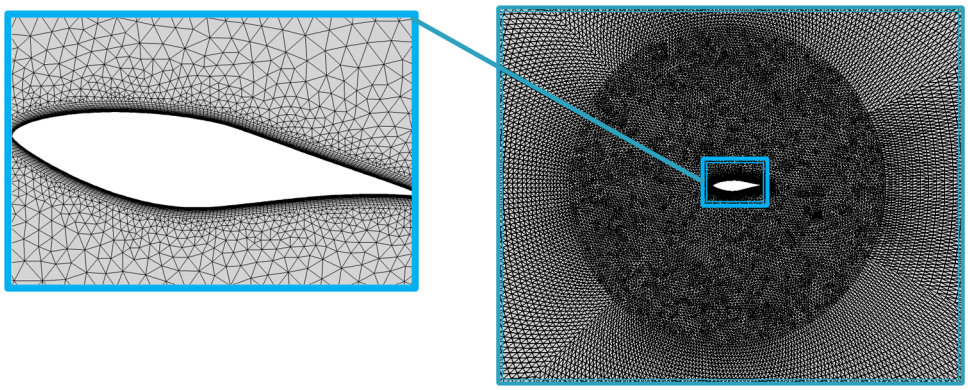

Fig. 4 Computational mesh for S802 aerofoil

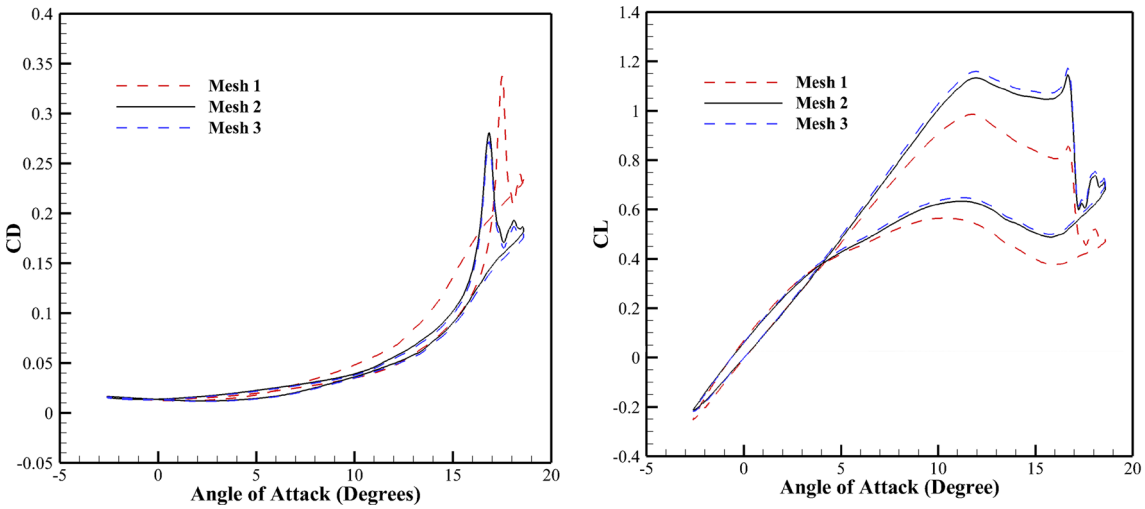

Fig. 5 Grid Independence for (i) coefficient of drag (ii) coefficient of lift

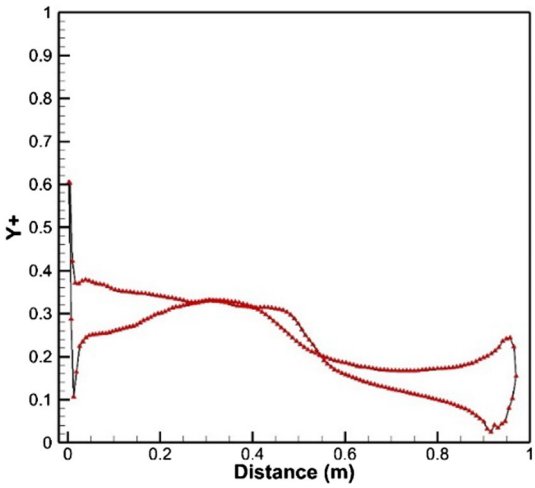

Fig. 6 Wall Y + distance for aerofoil S809 mesh

During the upward stroke for a higher angle of attack, the drag curve was over-predicted. The peak attained is similar to Mamouri et al. [31], but it has been predicted here for an angle before. At a large angle of attack, the lift coefficient is under-predicted by the current simulation, resulting in wider loops. The overall trend of the current result is the same as that of the validated results. For lower angles and the upstroke and down stroke motion of pitching for drag and lift curves, respectively, at higher angles, the present results yield maximum accuracy with the experimental results of Ramsay et al. [44]. The significant discrepancy is obtained at $\alpha > 18^{\circ}$, which comes due to vortex shedding on both leading and trailing edges. The interaction between the dynamic stall vortex and the trailing edge vortex at higher angles, both rotating in opposite directions, caused small eddies that led to a complex flow field.

6.2 Pressure Contours

Figure 8 shows the pressure contours and streamline for NREL S-809 aerofoil for different Re at four different angles: 18.6°, 8° upwards motion, 8° downward motion, and -2.6°. These are the mean and the peak angles for the pitching motion in one cycle for a reduced frequency of $K = 0.026$. Re 10^6 shows maximum pressure difference compared to lower

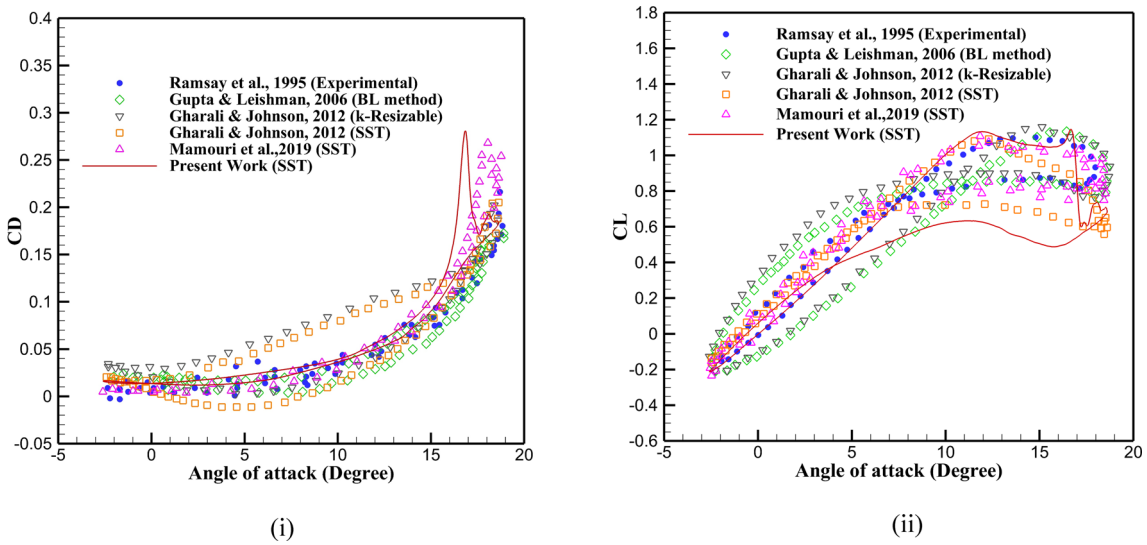

Fig. 7 Validation for (i) Coefficient of drag (ii) Coefficient of lift

Reynolds number as seen from the contour. The maximum angle of attack 18.6˚ shows the flow separation along the suction side of the aerofoil.

Here, a pair of vortices is observed instead of a single vortex near the tail of the aerofoil. The two vortices can be classified as primary and secondary vortices. There happens to be traction between the two vortices, causing vibratory load acting on the aerofoil. The stall produced due to a higher angle of attack seems to demolish once the angle reduces as the vortex strength decreases significantly and gets adhered to the suction side of the aerofoil near the tail. As the angle reduces further, the stalling is eliminated, and the flow occurs in a streamlined manner.

As the angle increases to 8°, an interesting phenomenon can be observed, where the flow still behaves in a streamlined manner, and there is no stall produced.

The vortex formation and mitigation are dependent on the angle of attack and the motion of the aerofoil. Also, there is a delay in stall angle for upward motion of aerofoil as compared to downward motion. The flow remains similar for a lower Reynolds number where the variation only occurs after the pitching motion exceeds the stall angle. The vortex formed for angle 18.6˚ tends to show variation in its orientation. As the Reynolds number decreases, the primary and secondary vortices tend to drift towards the downstream region. There is also a decrease in the size of the vortices for Reynolds number. This can be explained as the rate of fluid flow decreases, the ability to overcome the oscillating resistance due to aerofoil decreases, and the energy that can be damped from the kinetic energy of the fluid to the rotating lumped mass fluid, which leads to the shrinkage of the vortex. Figures 8 and 9 show the pressure and.

Streamlined contour for SD 7062 and NACA 0012 aerofoils respectively which shows similar flow characteristics of flow separation and stalling for aerofoils as of S-809. A change in the shape of the aerofoils majorly affects the shape and size of the vortex formed on the pressure sides. As the SD 7062 aerofoils has a higher thickness along the suction side near the nose of the aerofoils, it leads to more fluid adhering to the suction side leading to shrinkage in the vortex size as compared to S-809. The vortex covers the entire suction side for S-809, whereas the vortex development length is delayed for the SD 7062. The suction profile for NACA 0012 lies between the two aerofoils hence the vortex streamlines are moderate for the aerofoils.

6.3 Local Entropy Generation Contours

The local entropy generation contours are shown in Figs. 10, 11, 12 and 13 for S-809, SD 7062, and NACA 0012 aerofoils. Local entropy generation here despite its name represents the energy loss associated with the entropy generated rather than the entropy itself. The local entropy generation is shown for different pitching angles at different Reynolds numbers. The entropy generation can be sub-classified into two parameters, namely the strain rate and turbulent viscosity. The strain rate can be accounted for by the vorticity effect of the fluid which is caused due by chaotic wake. The turbulent viscosity variations are caused near the boundary due to abrupt slip between the stationery fluid along the surface and the free-stream fluid. The maximum entropy is observed at the maximum pitching angle when the vortices are present on the rear side. The entropy generation is detected along the surface as well as along the wake that denotes the presence of both strain rate and the turbulent viscosity variation. When the angle decreases to 8 deg, there is a substantial decrease in the entropy zone where the strain rate component is restricted near the tail of the aerofoils. This indicates that the strain

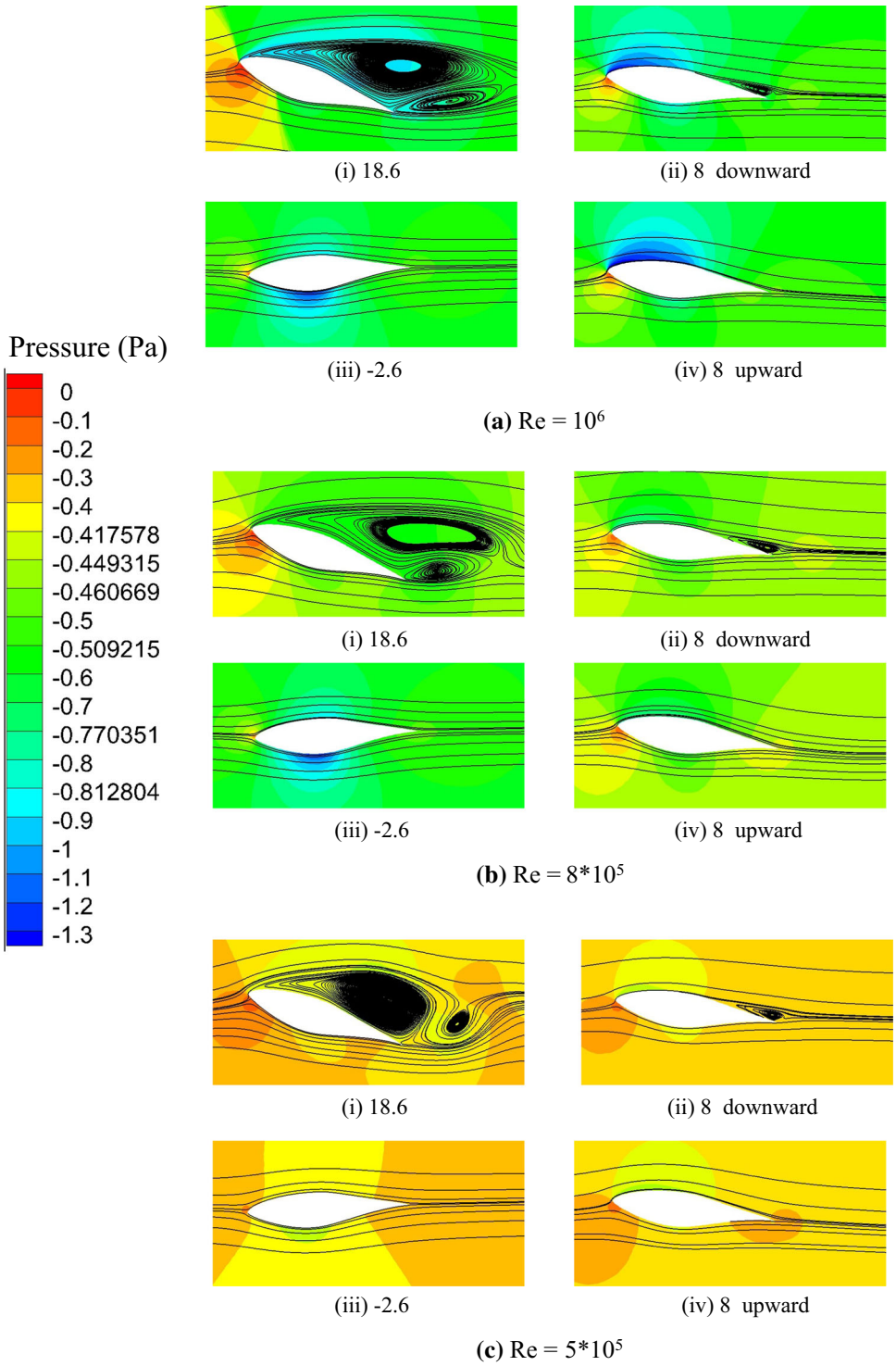

Fig. 8 Pressure contours for S-809 aerofoils for different Re and pitching angles

rate component is directly dependent on the vortices. As the angle decreases, due to streamlined flow, the turbulent viscosity variation is the only source of entropy generation. As the entropy generation is very low for these angles as compared to pitching angles above the stall angles, this shows that the strain rate is a more dominating factor for determining entropy generation. Due to the decrease in Re, there is a decrease in the vorticity and its energy trapping efficiency, which leads to a reduction in strain rate, hence a decrease in entropy generation.

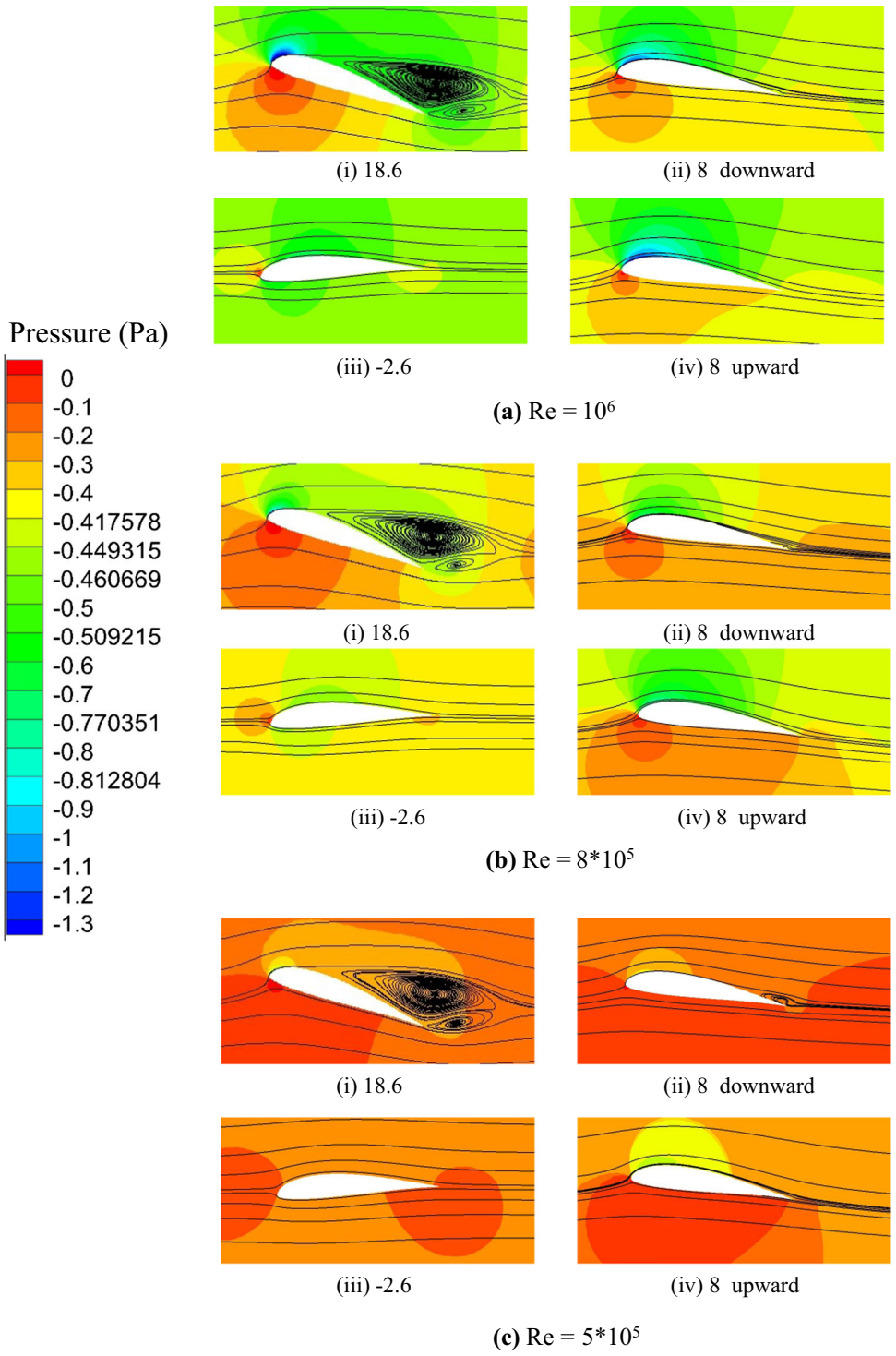

Fig. 9 Pressure contours for SD 7062 aerofoil for different Re and pitching angles

From Fig. 11, it can be seen that the entropy generation for angle 18.6° is maximum at the edges and decreases along the centre of the entropy mass. Here, the edges represent the tip of the vortices where the fluid revolves with maximum velocity producing maximum strain rate and the centre denotes the centre of the vortex where there is the highest fluid inactivity. A decrease in Reynolds number leads to the shifting of vortices towards the downstream region as discussed above. This can define the shift in the local entropy towards the downstream region. Comparing Fig. 13, there is an observation that the local entropy generated for the NACA 0012 is lesser than the subsequent aerofoils. The local entropy should not be confused with the total entropy. The vortices formed for NACA

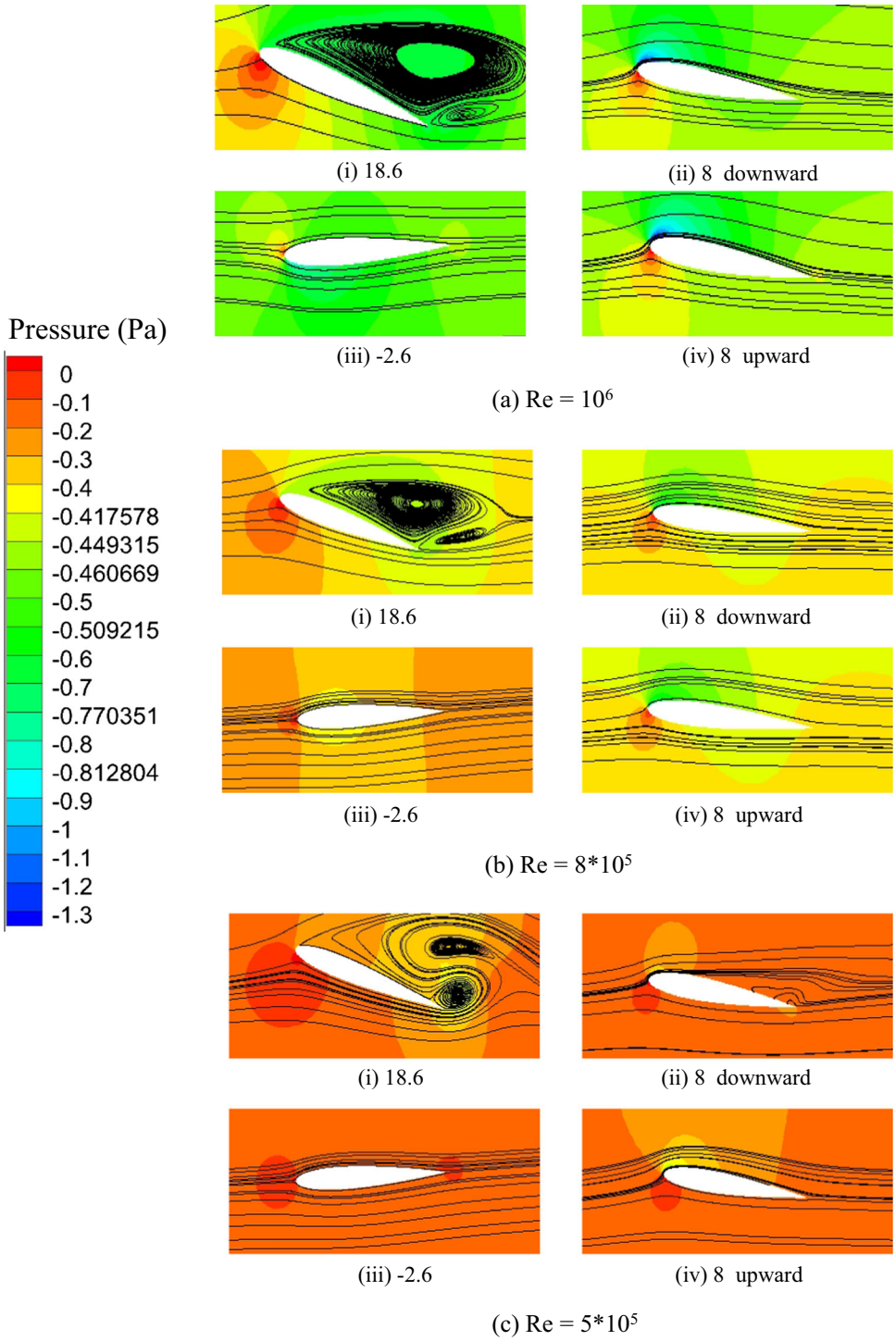

Fig. 10 Pressure contours for NACA 0012 aerofoil for different Re and pitching angles

0012 were larger which causes slower fluid circulation. This leads to a lower magnitude of the entropy generation of the strain rate. But the wake produced for this aerofoil ranges further downstream which leads to an extension of the entropy generated region for a larger area. Hence, despite having a lower magnitude of entropy generation which contributes to the local component, the total entropy generation is higher for NACA 0012 as compared to other aerofoils..

6.4 Drag and Lift Coefficients

Figure 14 shows the variation of drag and lift parameters with respect to time. Due to a constant angular frequency, there is a repetition of the curve for each 120.16 s. The hysteresis curve shown in Fig. 14 is initiated from the angle of attack 8 deg, while the blade makes upward progression. The lift initially decreases and then gradually decreases before

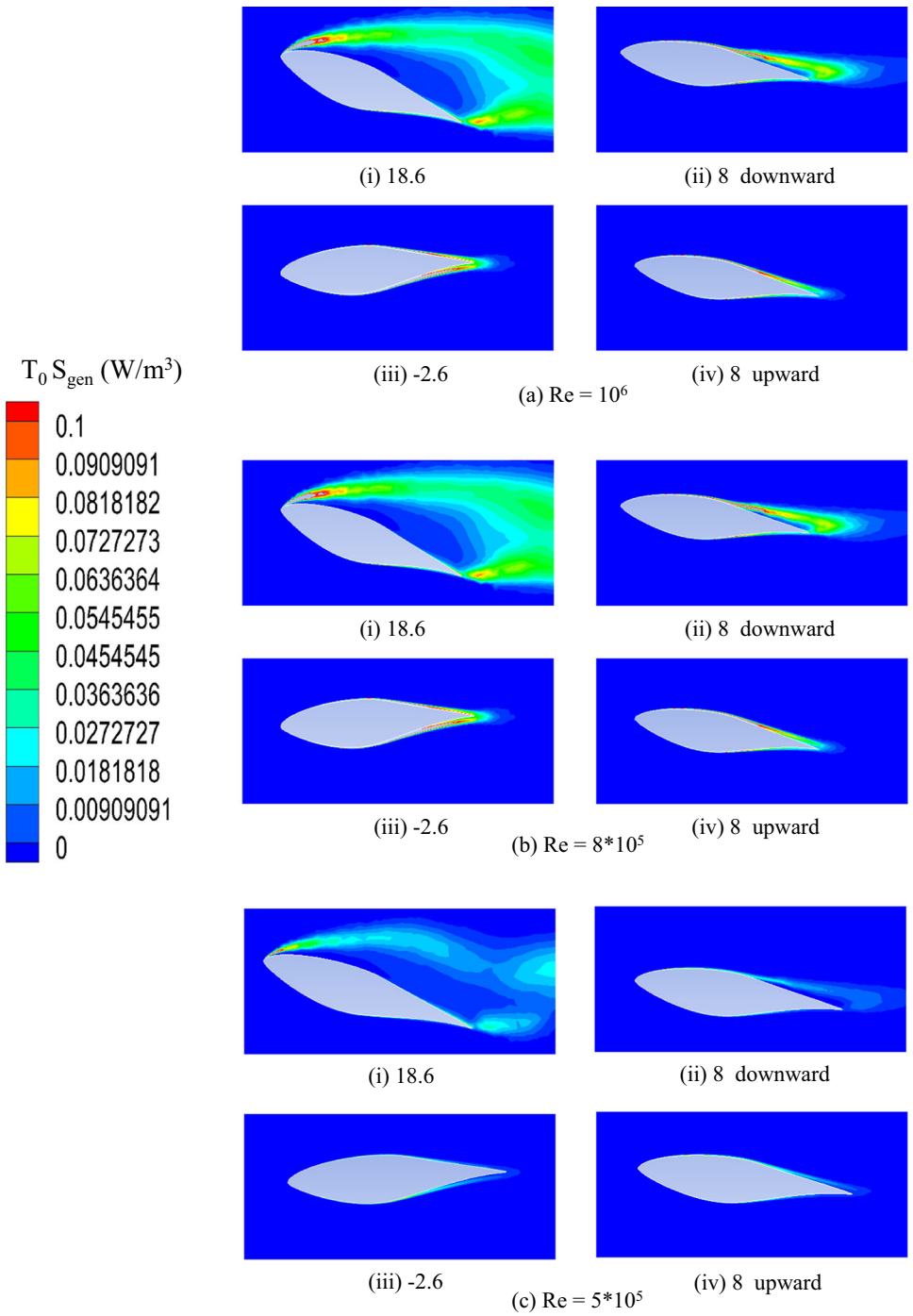

Fig. 11 Local entropy generation contours for S-809 aerofoil for different Re and pitching angles

attaining the peak angle 18.6° that shows the maximum lift is attained at an intermediate angle rather than the peak angle. The drag coefficient is the maximum for the peak angle. The drag and lift reduce drastically during the streamlined flow. There is some fluctuation observed for drag and lift coefficients near the peak angle which can be accounted for due to the abrupt rubbing between the primary and secondary vortices. Figure 14 shows a rather surprising result with the drag and lift coefficient tends to increase due to a decrease in the Re during the upward motion of the blade.

The case is opposite when the blade undergoes downward motion. This leads to the blade with the least Reynolds number covers the largest area of the hysteresis. The lift coefficient is maximum for SD 7062 followed by NACA 0012 (Fig. 14ii). SD 7062 shows a smoother curve for both drag and lift parameters, which can be accounted for its shape where the suction side acts like a bulged region that reduces

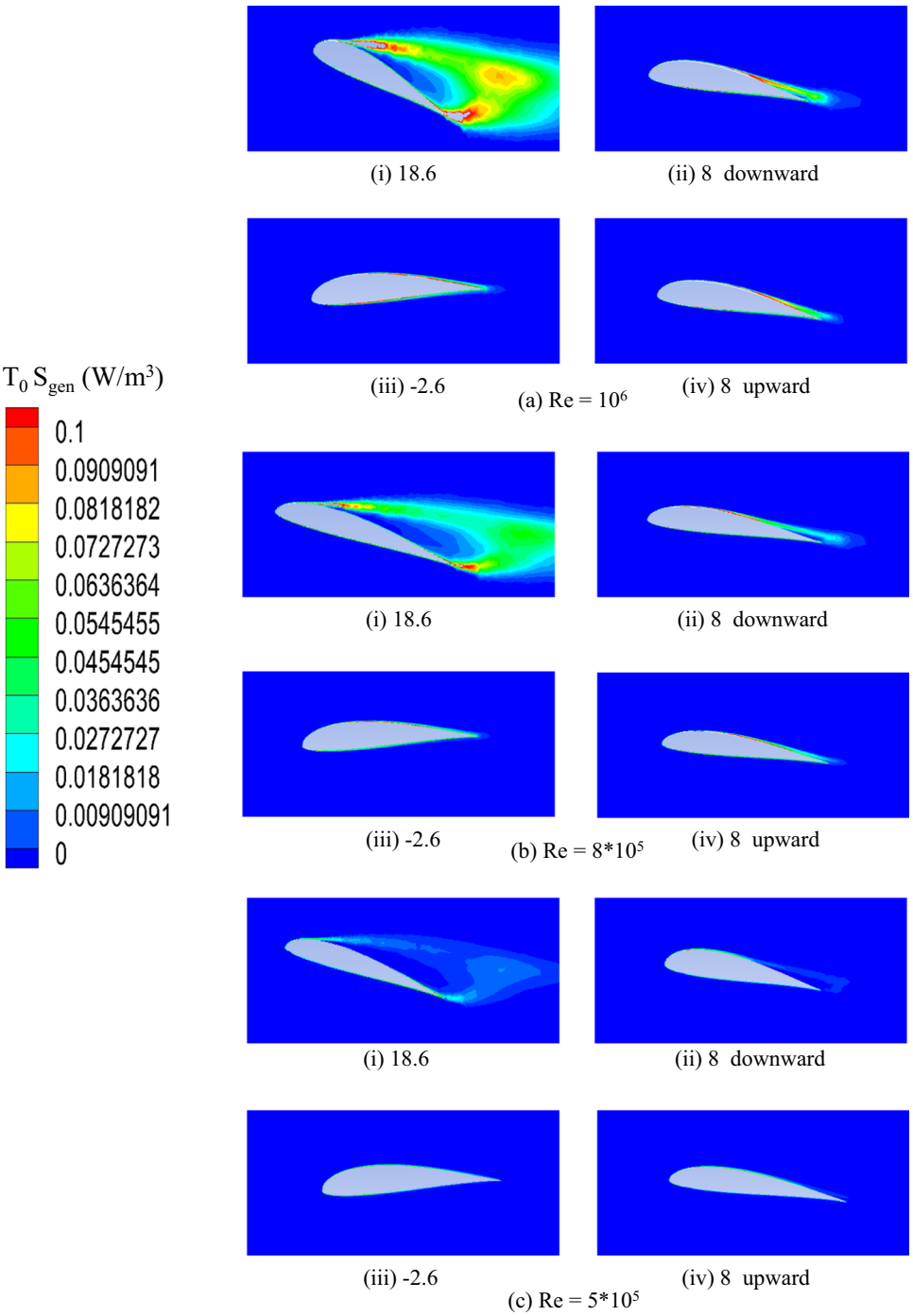

Fig. 12 Local entropy generation contours for SD-7062 aerofoils for different Re and pitching angles

the vortex generation, and the pressure side which acts like a cusp that provides the additional thrust for the lift. A larger lift coefficient is desirable as it accounts for larger useful work production of aerofoils. The aerofoils have the least drag coefficient, and the other two blades show a higher value. Here, the drag coefficient highly determines the vortex generated along the rear side of the blade, and it is more favourable for the entropy generation.

6.5 Total Entropy Generation

Figure 15(i) shows the total entropy generated for different aerofoils. The total entropy generated is calculated by taking area and time-weighted integral for local entropy generated data. The non-dimensional form of the parameter is obtained by taking the value for S-809 at Re 10^6 and dividing it with other parameters to obtain a comparative study. As shown, the entropy generated for NACA 0012 is almost double the

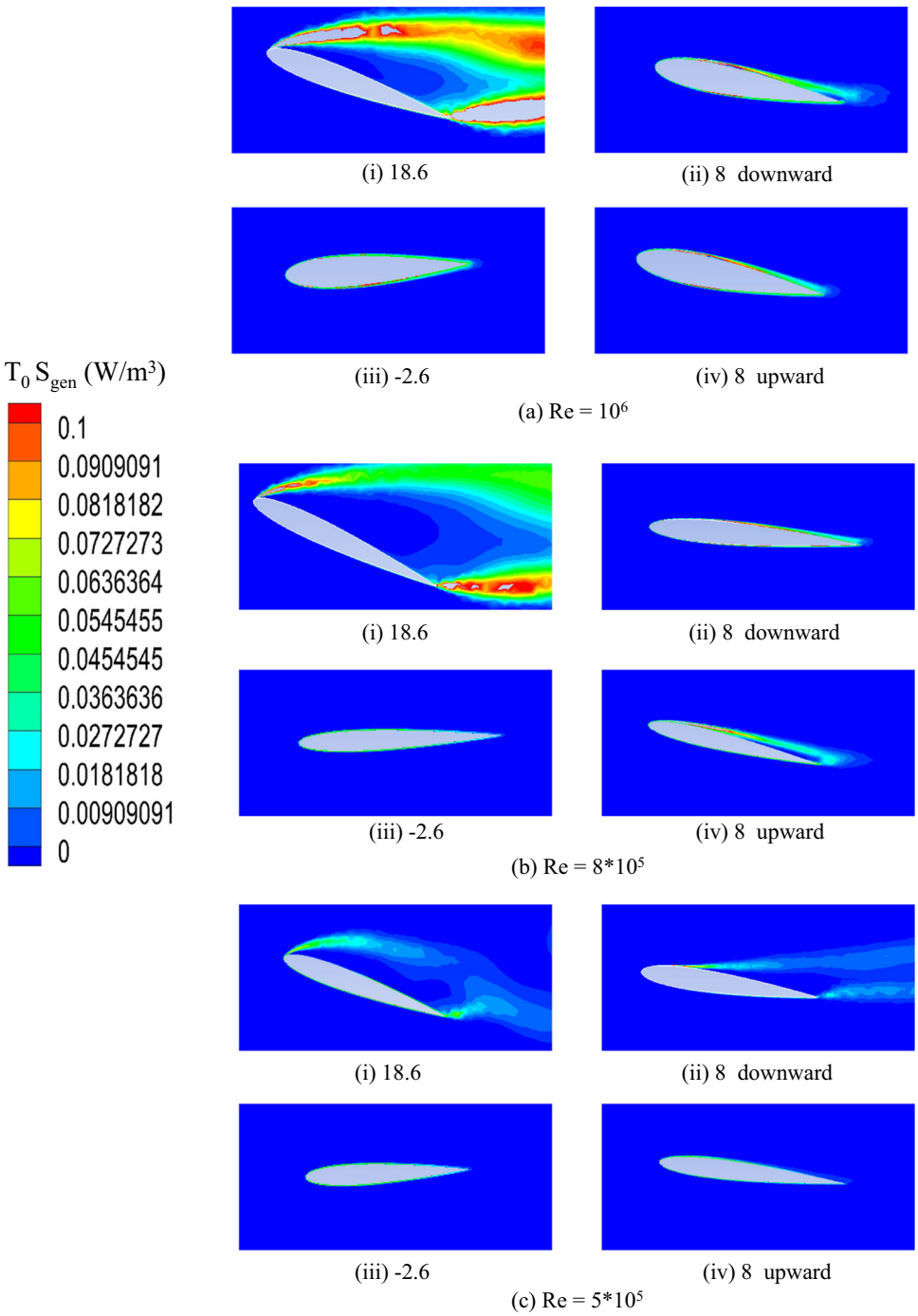

Fig. 13 Local entropy generation contours for NACA 0012 aerofoil for different Re and pitching angles

value for the other aerofoils. There is a minor difference, but the S-809 has the least entropy generation. Figure 15ii shows the effective work chart which is a function of the effective lift coefficient. This parameter is also dimensionless with the parameters divided by S-809 at Re 10^6. SD 7062 shows maximum effective work done, with a variation of about 2.46 times with respect to S-809 at Re 10^6 which means that the SD 7062 aerofoil has produced more effective work than the other aerofoils.

The curves do not show linearity towards Re, particularly the entropy generation rate shows an increase in the slope after Re $8*10^5$. This can be contributed to the fact that at the lower range of Re, the flow is still in the transition region from laminar to turbulent and at Re 10^6 the flow attains complete turbulence. The increase in the component of turbulence causing an increase in fluctuating component of the velocity and increase in the dissipation energy provides apt justification for the increment in slope. The transition is not imminent

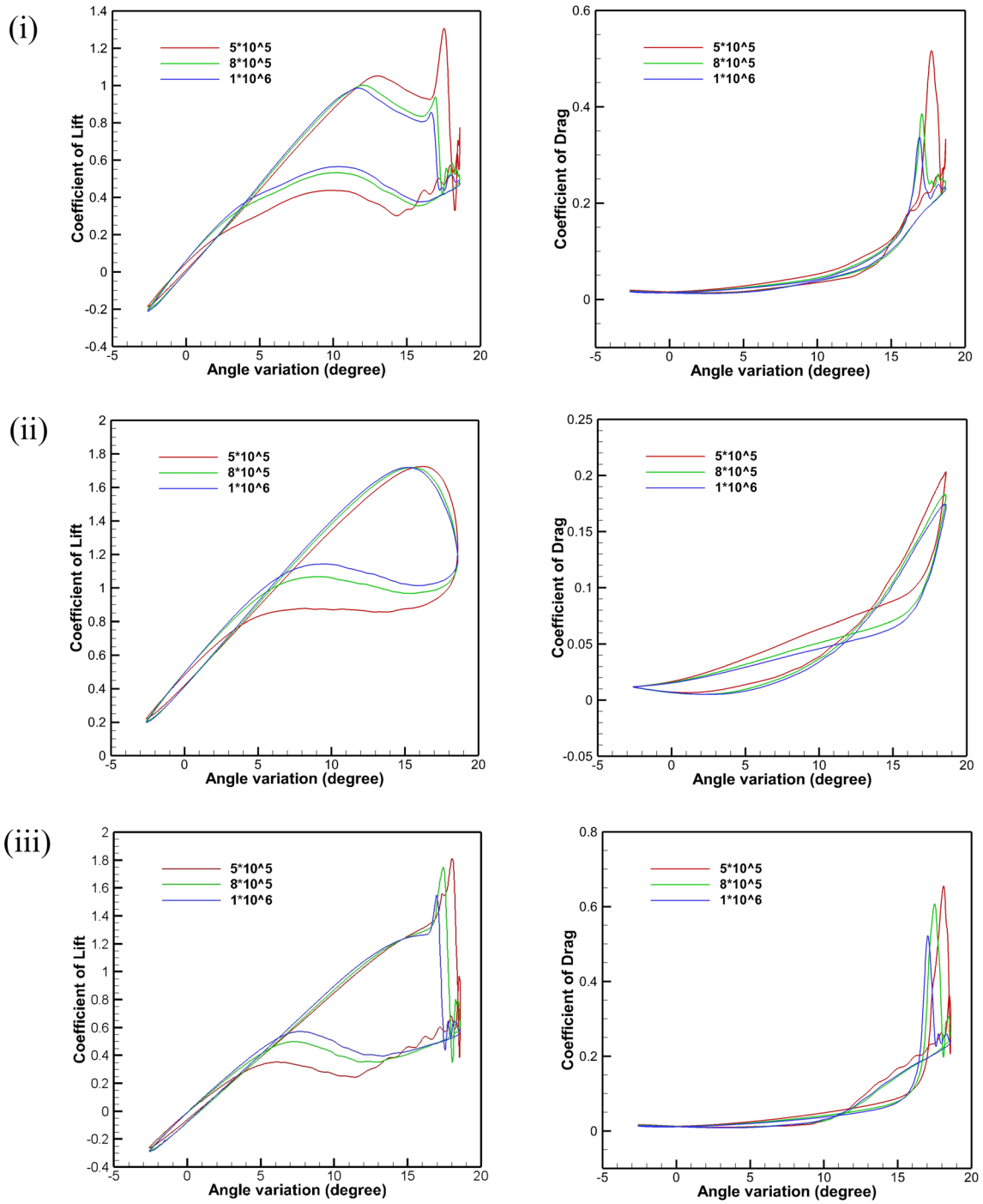

Fig. 14 Lift and drag coefficient variation with respect to angle for (i) S809 and (ii) SD7062 and (iii) NACA 0012

for the effective work graph due to its dependency on only the aerodynamic constants but not on the strain rate of the turbulent dissipative energy term. There is also a variation in the slope of the parameters for different profiles highlighting the influence of blade profile on the flow and energy distribution. NACA 0012, due to its plain and symmetric profile, provides lesser resistance to vortex mitigation and dynamic wake formed, and the vortex spans for the entire profile leading to a larger value of entropy generation among the others. The SD 7062 blade on the other hand has s smoother profile than the S-809 and an up-liftment towards the upper portion of the blade giving an asymmetrical profile. This up-liftment causes the point of contact along the lower portion generating force in the direction of the lift. The force acting on the

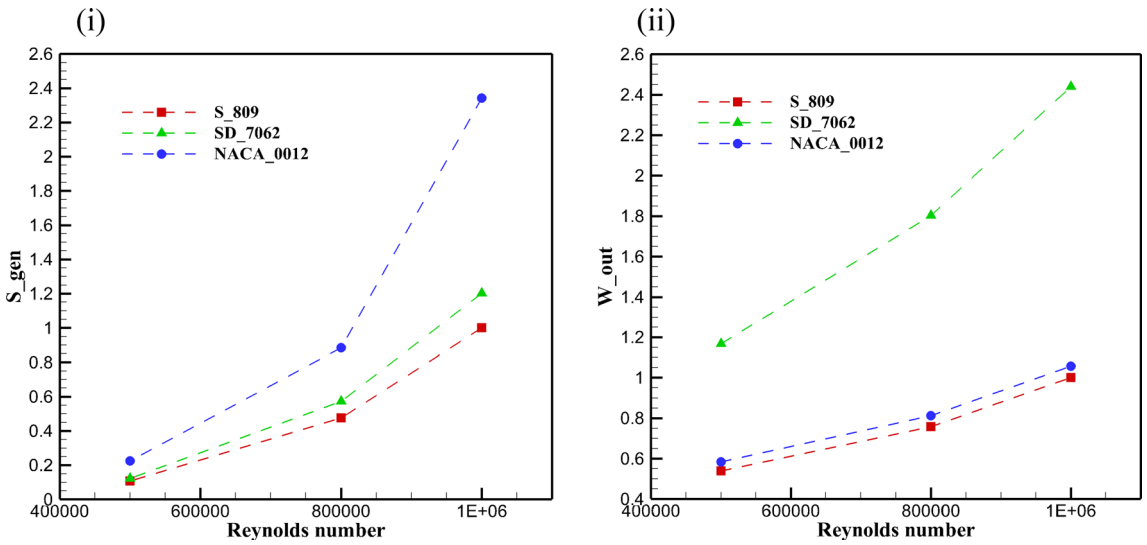

Fig. 15 (i) Entropy generation and (ii) effective work variation with Re for different aerofoils

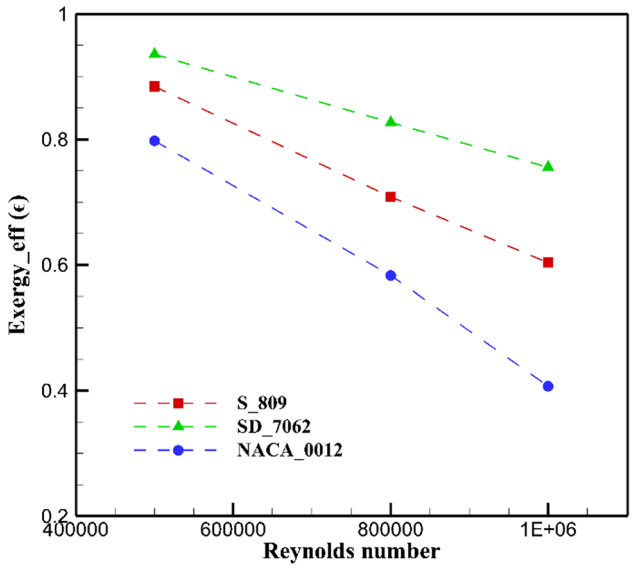

Fig. 16 Exergy efficiency variation with Re for different aerofoils

point of contact increases as the Re increases, increasing the lift and the effective work generated through the profile.

6.6 Exergy Efficiency

The exergy efficiency is the function of the entropy generation and the effective work done by the blades. The exergy efficiency or the second law efficiency is an essential performance parameter for turbo-machinery design, which measures the quality of the energy obtained and the irreversibility involved in the system. An interesting pattern is shown in Fig. 16 where the variation of exergy efficiency shows more linearity with the Re than the entropy generation, and effective work is done curves as shown in Fig. 15. The efficiency is maximum for SD 7062 around 93% and is minimum for NACA 0012 around 39% throughout the Re range. The efficiency is directly related to the effective work done and decreases by the entropy generated in the system. With the increase in Re, there is a decrease in ϵ which shows it is more influenced by the entropy generation rate. The S_{gen} is dependent on the strain rate, which is in the power of two for the velocity gradients which explains nonlinearity with Re. The S_{gen} the term also depends on the turbulent diffusion rate that increases with the increase in turbulence in the flow.

The rise of entropy generation rate with Re is more than the effective work. The slope of decrement with an increase in Re varies for the aerofoil profile, with NACA 0012 having the steep slope among all blades. The aforementioned results confirm that the NACA 0012 shows maximum entropy generation among all, and the exergy efficiency is affected more by the entropy rather than the effective work.

7 Conclusion

The numerical simulations were produced for three wind turbine aerofoils, NACA0012, S-809, and SD 7062, to determine the entropy generation characteristics. The simulation was produced for oscillating aerofoil blades at a reduced frequency of 0.026 for Reynolds numbers $5*10^5$ to 10^6. The entropy generation rate obtained was used to find a relation between the aerodynamic forces and to incorporate the effect of the unsteady wake formed in the accurate estimation of the dynamic stall. The results obtained were:

- The drag hysteresis curves show that the drag coefficient lowers for SD7062 as the flow separation does not occur compared to S809 and NACA 0012. The drag coefficient decreases with an increase in Reynolds number.
- Lift force increases at higher angles but decreases for angles where stalling is initiated. The curve shows a smoother profile delay in flow separation for SD 7062 with a higher lift force acting along the blade. A decrease in Re shows a delay in stalling and an increase in the magnitude of lift force.
- The entropy generation depends more on the strain rate. Due to a higher strain rate with an increase in Reynolds number, entropy generation increases. S_{gen} is maximum for NACA 0012. The entropy generation is related to the dynamic stalling along with the drag forces, proving to be a reliable criterion for estimation of a dynamic stall than the drag coefficient.
- The total entropy generation increases with an increase in Re, where it is affected by the velocity and turbulence of fluid. The correlation with Re is also affected by the aerofoils blade profile with NACA 0012 shows higher variation in S_{gen} with Re increment.
- The effective work produced by the aerofoils is the maximum for SD 7062 as the losses due to irreversibility are the least. The effective work is found to be directly related to the lift coefficient and increased linearly with Re.
- The exergy efficiency shows linear decrement with the increase in Re. It has more influence on the total entropy generation than the effective work done. The SD 7062 is the most efficient aerofoils blade with around 93% efficiency for Re $5*10^5$. The NACA 0012 is the least efficient blade, with a low efficiency of 39% at Re 10^6.

The optimum aerofoil design can be selected based on the exergy efficiency shown by a blade when compared with blades under same conditions. This can help the designers to determine the second law efficiency and thermodynamic performance evaluation of the wind turbine. The entropy generation and exergy efficiency can produce accurate quantified data for the dynamic stall angle and flow separation that can be beneficial for offshore designers. Also, quantifying the exergy could provide a strong tool for designers to quantify the energy losses. The entropy generation also shows linear dependence with drag coefficient and effective work output is inverse of the entropy generation rate, hence it can be preferred over the conventional aerodynamic constants to estimate dynamic stall.

Understanding dynamic stall in pitching aerofoils using entropy generation method sets the stage for future studies on exploring the influence of higher Reynolds numbers in the transonic and supersonic range, at an unsteady free-stream flow and for a higher range of reduced aerofoils frequencies.

Supplementary Information The online version contains supplementary material available at https://doi.org/10.1007/s13369-022-07424-x.

Acknowledgements This research is supported by the Product Development Laboratory and the Computational Fluid Dynamics Laboratory of the SRM Institute of Science and Technology. These supports are gratefully acknowledged.

Declarations

Conflict of interest We confirm that the manuscript has been read and approved by all named authors and that there are no other persons who satisfied the criteria for authorship but are not listed. We further confirm that the order of authors listed in the manuscript has been approved by all of us.

References

1. Zhao, Y.; Cheng, Z.; Sandvik, P.C.; Gao, Z.; Moan, T.: An integrated dynamic analysis method for simulating installation of single blades for wind turbines. Ocean. Eng. **152**, 72–88 (2018)
2. Castellani, F.; Astolf, D.; Garinei, A.; Proietti, S.; Sdringola, P.; Terzi, L.; Desideri, U.: How wind turbines alignment to wind direction affects effciency? A case study through SCADA data mining. Energy Procedia **75**, 697–703 (2015)
3. Li, X.; Zhang, L.; Song, J.; Bian, F.; Yang, K.: Aerofoil design for large horizontal axis wind turbines in low wind speed regions. Renew. Energy **145**, 2345–2357 (2020)
4. Liu, P.; Yu, G.; Zhu, X.; Du, Z.: Unsteady aerodynamic prediction for dynamic stall of wind turbine aerofoils with the reduced order modeling. Renew. Energy **69**, 402–409 (2014)
5. Yan, C.; Archer, C.Y.: Assessing compressibility effects on the performance of large horizontal-axis wind turbines. Appl. Energy **212**, 33–45 (2018)
6. Chan, C.H.; Bai, H.L.; He, D.Q.: Blade shape optimization of the Savonius wind turbine using a genetic algorithm. Appl. Energy **213**, 148–157 (2018)
7. Wernert, P.; Geissler, W.; Raffel, M.; Kompenhans, J.: Experimental and numerical investigations of dynamic stall on a pitching aerofoil. AIAA J. **34**(5), 982–989 (1996)
8. Soltani, M.R.; Mahmoudi, M.: Measurements of velocity field in the wake of an oscillating wind turbine blade. Aeronaut. J. **114**(1158), 493–504 (2010)
9. Akbari, M.H.; Price, S.J.: Simulation of dynamic stall for a NACA 0012 aerofoil using a vortex method. J. Fluids Struct. **17**, 855–874 (2003)
10. Rezaeiha, A.; Kalkman, I.; Blocken, B.: Effect of pitch angle on power performance and aerodynamics of a vertical axis wind turbine. Appl. Energy. **197**, 132–150 (2017)
11. Cui, A.; Knight, D.D.: Parallel computation of the 2-d navier-stokes flowfield of a pitching aerofoil. Int. J. Comput. Fluid Dyn. **4**(1–2), 111–135 (2007)
12. Gharali, K.; Johnson, D.A.: Dynamic stall simulation of a pitching aerofoil under unsteady freestream velocity. J. Fluids Struct. **42**, 228–244 (2013)
13. Gharali, K.; Johnson, D.A.: Effects of nonuniform incident velocity on a dynamic wind turbine aerofoil. Wind Energy **18**(2), 237–251 (2014)
14. Gharali, K.; Johnson, D.A.; Lam, V.; Gu, M.: A 2D blade element study of a wind turbine rotor under yaw loads. Wind Eng. **39**(5), 557–567 (2015)
15. Gharali, K.; Gharaei, E.; Soltani, M.; Raahemifar, K.: Reduced frequency effects on combined oscillations, angle of attack and

free stream oscillations, for a wind turbine blade element. Renew. Energy **115**, 252–259 (2018)
16. Gharali, K.; Johnson, D.A.: Numerical modeling of an S809 aerofoil under dynamic stall, erosion and high reduced frequencies. Appl. Energy **93**, 45–52 (2012)
17. Wilcox, D.C.: Turbulence Modeling for CFD. DCW Industries Inc, La Canada, California (1998)
18. Menter, F.R.: Two-equation eddy-viscosity turbulence models for engineering applications. AIAA J. **32**(8), 1598–1605 (1994)
19. Xu, H.Y.; Qiao, C.L.; Ye, Z.Y.: Dynamic stall control on the wind turbine aerofoil via a Co-flow jet. Energies **9**, 429–454 (2016)
20. Liu, X.; Lu, C.; Liang, S.; Godbole, A.; Chen, Y.: Vibration-induced aerodynamic loads on large horizontal axis wind turbine blades. Appl. Energy. **185**, 1109–1119 (2016)
21. Bejan, A.: A study of entropy generation in fundamental convective heat transfer. J. Heat Transf. **101**(4), 718 (1979)
22. Bejan, A.: Second law analysis in heat transfer. Energy **5**(8–9), 720–732 (1980)
23. Wenterodt, T.; Redecker, C.; Herwig, H.: Second law analysis for sustainable heat and energy transfer: The entropic potential concept. Appl. Energy. **139**, 376–383 (2015)
24. Vatanmakan, M.; Lakzian, E.; Mahpeykar, M.R.: Investigating the entropy generation in condensing steam flow in turbine blades with volumetric heating. Energy **147**, 701–714 (2018)
25. Walsh, E.J.; McEligot, D.: Relation of entropy generation to wall 'laws' for turbulent flows. Int. J. Comput. Fluid Dyn. **22**(10), 649–657 (2008)
26. Foroozesh, F.; Khoshnevis, A.B.; Lakzian, E.: Improvement of the wet steam ejector performance in a refrigeration cycle via changing the ejector geometry by a novel EEC (Entropy generation, Entrainment ratio, and Coefficient of performance) method. Int. J. Refrig **110**, 248–261 (2020)
27. Shehata, A.S.; Xiao, Q.; Saqr, K.M.; Alexander, D.: Wells turbine for wave energy conversion: a review. Int. J. Energy Res. **41**(1), 6–38 (2016)
28. Wen, C.; Zhang, J.; Wang, C.; Dong, X.; Peng, H.; Gao, H.; Wang, J.: An analysis method for exergy efficiency of wind turbines based on experiment and simulation. Energy Sources Part A Recov. Util. Environ. Effects **42**(9), 1072–1084 (2020)
29. Mortazavi, M.; Sobhgahi, S.: Numerical investigation on the exergetic performance of NREL aerofoil families for wind turbine application. Int. J. Exergy **18**, 387 (2015)
30. Mamouri, A.R.; Khoshnevis, A.B.; Lakzian, E.: Entropy generation analysis of S825, S822, SD7062 offshore wind turbine aerofoil geometries. Ocean. Eng. **173**, 700–715 (2019)
31. Mamouri, A.R.; Lakzian, E.; Khoshnevis, A.B.: Entropy analysis of pitching aerofoil for offshore wind turbines in the dynamic stall condition. Ocean Eng. **187**, 106229 (2019)
32. Mamouri, A.R.; Khoshnevis, A.B.; Lakzian, E.: Experimental study of the effective parameters on the offshore wind turbine's aerofoil in pitching case. Ocean. Eng. **198**, 106955 (2020)
33. Karthikeyan, N.; Kalidas Murugavel, K.; Arun Kumar, S.; Rajakumar, S.: Review of aerodynamic developments on small horizontal axis wind turbine blade. Renew. Sustain. Energy Rev. **42**, 801–822 (2015)
34. Gross, A.; Fasel, H.F.: Flow control for NREL S822 wind turbine aerofoil. AIAA J. **50**(12), 2779–2789 (2012)
35. Gupta, S.; Leishman, J.G.: Dynamic stall modeling of the S809 aerofoil and comparison with experiments. Wind Energy **9**(6), 521–547 (2006)
36. Guillaud, N.; Balarac, G.; Goncalves, E.: Large Eddy Simulations on a pitching aerofoil: analysis of the reduced frequency influence. Comput. Fluids **161**, 1–13 (2018)
37. Hand, B.; Kelly, G.; Cashman, A.: Numerical simulation of a vertical axis wind turbine aerofoil experiencing dynamic stall at high Reynolds numbers. Comput. Fluid **149**, 12–30 (2017)
38. Zhong, J.; Li, J.; Guo, P.; Wang, Y.: Dynamic stall control on a vertical axis wind turbine aerofoil using leading-edge rod. Energy **174**, 246–260 (2019)
39. Versteeg, H.K.; Malalasekera, W.: An Introduction to Computational Fluid Dynamics. Pearson Education Limited, London (2007)
40. Sayed, M.A.; Kandil, H.A.; Shaltot, A.: Aerodynamic analysis of different wind turbine-blade profles using fnite-volume method. Energy Convers. Manag. **64**, 541–550 (2012)
41. Kock, F.; Herwig, H.: Local entropy production in turbulent shear flows: a high-Reynolds number model with wall functions. Int. J. Heat Mass Transf. **47**(10–11), 2205–2215 (2004)
42. Herwig, H.; Kock, F.: Direct and indirect methods of calculating entropy generation rates in turbulent convective heat transfer problems. Heat Mass Transf. **43**(3), 207–215 (2006)
43. ANSYS Inc. ANSYS FLUENT 12.0 (Theory Guide); (2009)
44. Ramsay, R.; Homan, M.; Gregorek, G.: Effects of grit roughness and pitch oscillation on the S809 aerofoil. Tech. Rep., NREL. NREL/TP-442–7817 (1995)